A consistent radio to sub-mm pc-scale study of the nucleus of NGC 1068

N.B. When citing this work, cite the original published paper.

(article starts on next page)

A consistent radio to sub-mm pc-scale study of the nucleus of NGC 1068

Isaac M. Mutie [1,2]★ Santiago del Palacio [3] Robert J. Beswick,[2] David Williams-Baldwin [2]
Jack F. Gallimore,[4] John S. Gallagher,[5,6] Susanne E. Aalto[3] and Paul O. Baki[1]

[1]*Department of Astronomy and Space Science, Technical University of Kenya, P.O Box 52428-00200, Nairobi, Kenya*
[2]*Jodrell Bank Centre for Astrophysics, School of Physics and Astronomy, The University of Manchester, Manchester M13 9PL, UK*
[3]*Department of Space, Earth and Environment, Chalmers University of Technology, SE-412 96 Göteborg, Sweden*
[4]*Department of Physics and Astronomy, Bucknell University, Lewisburg, PA 17837, USA*
[5]*Department of Physics and Astronomy, Macalester College, 1600 Grand Ave, Saint Paul, MN 55105, USA*
[6]*Department of Astronomy, University of Wisconsin–Madison, 475 North Charter Street, Madison, WI 53706, USA*

ABSTRACT

The origin of radio emission in radio-quiet (RQ) active galactic nucleus (AGN) remains a long-standing mystery. We present a detailed study of the cm to sub-mm emission from the nucleus of the nearby prototypical RQ Seyfert 2 galaxy, NGC 1068. We analyse observations between 4.5 and 706 GHz using e-MERLIN, VLA, and ALMA. We restricted all data used for imaging to a matching $uv-$range of $15-3300$ kλ, to ensure that all data sampled the same spatial scales. All images were restored with a $\sim$0.06 arcsec beam. To derive the spectral energy distribution (SED), we fit synchrotron, free–free, dust, and coronal component models to these data. We report that the sub-mm excess between $\sim$200 and 700 GHz is consistent with synchrotron emission from a compact and optically thick corona with a radius $R_c \approx 70 \pm 5\ R_g$, a fraction of $\sim$10 $\pm$ 2 per cent of the energy density in the form of non-thermal electrons, and a magnetic field strength $B \approx 148$ G. The luminosity of the corona is roughly consistent with – though higher than – the expected from mm–X-ray correlations derived in recent studies of RQ AGNs. This difference is likely due to the corona SED peaking at ($\approx$550 GHz). Between 10 and $\sim$200 GHz, the SED is dominated by free–free emission. High angular resolution observations at frequencies below 5 GHz are needed to constrain a putative optically thin synchrotron component and the amount of free–free absorption.

Key words: radiation mechanisms: general – galaxies: active – galaxies: jets.

1 INTRODUCTION

The NGC 1068 is a nearby prototypical radio-quiet (RQ) Seyfert 2 galaxy, with redshift (z) = 0.00379, optical velocity $V_{optical}$ = 1148 km s^{-1}, and spatial scale = 72 pc arcsec^{-1} (Tully 1988; Capetti et al. 1995; Bland-Hawthorn et al. 1997). The accretion disc of NGC 1068 and the broad-line region (BLR) are obscured by a thick dusty, molecular torus detected only by spectropolarimetry (Antonucci & Miller 1985; Mason et al. 2006; Ramos Almeida & Ricci 2017; Imanishi et al. 2018). NGC 1068 has become the archetype for obscuration-based unifying models (Antonucci 1993). The X-ray emission measured by *NuSTAR*, *XMM–Newton*, and *Chandra* is largely attenuated and variable, indicating that the obscuring medium is Compton-thick and clumpy (Young, Wilson & Shopbell 2001; Mason et al. 2006; Capetti et al. 2013; Marinucci et al. 2016).

A flat-spectrum radio source, dubbed S1, marks the location of a supermassive black hole (SMBH) on 20-mas ($\sim$1.4 pc) scales (Gallimore et al. 1996, 2024). Very Long Baseline Array (VLBA) observations resolve the continuum source into an elongated pc-scale structure oriented nearly at right angles to the kpc-scale radio

jet (which is nearly north–south). The morphology of S1 has been interpreted as a plasma torus (Gallimore, Baum & O'Dea 2004) located inside the obscuring molecular torus resolved by ALMA (Imanishi, Nakanishi & Izumi 2016; García-Burillo et al. 2019; Impellizzeri et al. 2019).

At radio–sub-mm wavelengths, S1 (see Fig. 1) has a peculiar continuum spectrum compared to the central radio sources in other Seyfert nuclei of comparable active galactic nucleus (AGN) luminosity. Typically, radio emission in Seyfert nuclei is attributed to steep-spectrum synchrotron emission (e.g. Ulvestad & Wilson 1989); however, the cm-wave spectrum of S1 is flat, steep, or inverted depending on the angular resolution of the interferometric observations used to derive the flux density. In other words, the radio emission of S1 has a complicated morphology and is resolved on all scales, and comparing data sets with very widely varying $uv-$coverage and angular resolution has so far only led to conflicting results (e.g. Ulvestad & Wilson 1989; Gallimore et al. 2004; Krips et al. 2006; Inoue, Khangulyan & Doi 2020; Baskin & Laor 2021; Michiyama, Inoue & Doi 2023). As a result, it has been challenging to construct a reliable spectral energy distribution (SED) for the nuclear radio source S1, and understanding the emission mechanism(s) responsible for the radio continuum has remained a long-standing problem.

★ E-mail: mumoisaac@gmail.com
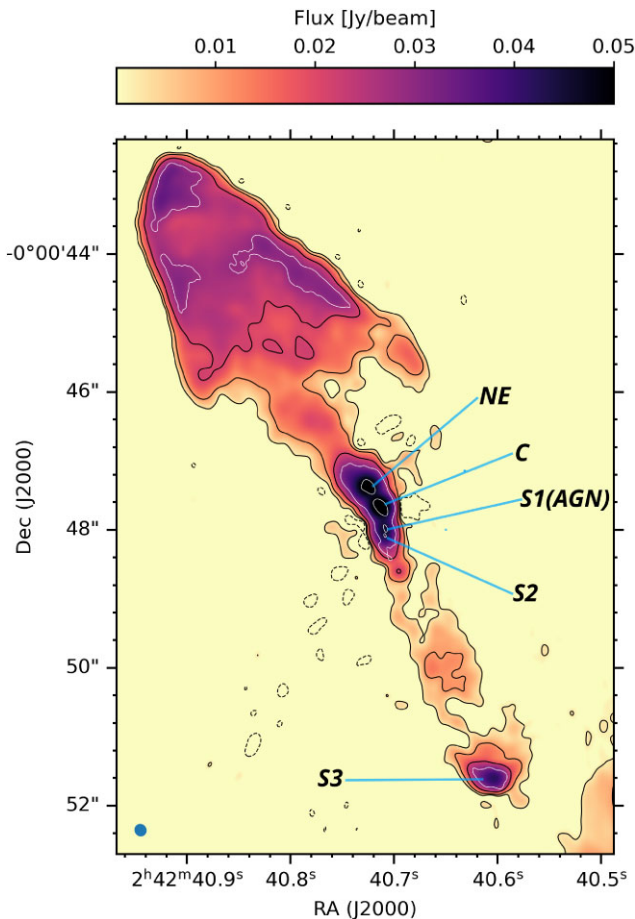
Figure 1. Image of the inner jet in NGC 1068, showing the AGN (S1) and the compact jet components in context, taken from Mutie et al. (2024). The composite image is constructed from combining *e*-MERLIN + VLA data between 4 and 12 GHz yielding angular resolution scales between 0.18 and 0.05 arcsec with rms sensitivity of 30 μJy beam^{-1}.

need to measure the SED with sufficiently high, matching angular resolution and *uv*-coverage.

Identifying the origin of the S1 radio continuum source of NGC 1068 is fundamental to our understanding of the obscuring region surrounding the AGN. The nature of S1 must be intimately tied to the heating, dynamics, and resulting geometry of the molecular torus, all of which are central to understanding AGN unified schemes. In particular, synchrotron emission from an optically thick corona can be expected to produce a 'bump' in the mm/sub-mm SED (e.g. Inoue & Doi 2014; Behar et al. 2015; Ricci at al. 2023; Shablovinskaya et al. 2024); such a spectral feature has already been suggested in NGC 1068 (Inoue et al. 2020; Michiyama et al. 2023). Proper modelling of this component can yield reliable estimates of the coronal size, non-thermal particle content, and magnetic field strength. These characterizations can then be used to improve the recent proposition that neutrinos detected in NGC 1068 (Aartsen et al. 2020) originate in the X-ray corona (Inoue et al. 2020; Eichmann et al. 2022; Padovani et al. 2024), in the vicinity of the $(1.2–1.7) \times 10^7 \, M_\odot$ SMBH hosted by NGC 1068 (Greenhill & Gwinn 1997; GRAVITY Collaboration 2020; Gallimore et al. 2024). Recent studies have proposed that neutrinos can be produced within the X-ray corona because accelerated electrons and protons in the coronae can generate gamma-rays and neutrinos through inverse-Compton scattering, *pp* and *pγ* interactions (Inoue & Doi 2018; Inoue et al. 2019; Inoue et al. 2020).

In this paper we use data from the *enhanced*-Multi Element Linked Interferometer Network (*e*-MERLIN), the Karl G. Jansky Very Large Array (VLA), and the Atacama Large Millimeter/sub-millimeter Array (ALMA) to obtain a complete radio–sub-mm SED with data points between 4.5 and 706 GHz, with matched angular resolution (∼0.06 arcsec) and *uv*−range (15−3300 kλ). In addition, we include complementary data at 1.4 GHz from the *e*-MERLIN to further constrain the SEDs at lower frequencies.

The structure of this paper is as follows: in Section 2 we present the calibration, reduction, and imaging of the data. In Section 3 we discuss the SED fitting model. In Section 4 we discuss the results obtained. In Section 5 we conclude from our findings and discuss future work.

2 OBSERVATIONS, DATA REDUCTION, AND IMAGING

The *e*-MERLIN data were observed on 2022 March 24, 25, 28; April 22; and May 20 and 22, under project code CY13006. A total of 24 spectral windows (spws) were observed, each with a bandwidth of 128 MHz. Each observing epoch covered 4 spws spanning 512 MHz, from 4.5 to 7.5 GHz and were centred at 4.8, 5.3, 5.8, 6.3, 6.8, and 7.3 GHz, respectively. Observations for the 3rd epoch (March 28) were unsuccessful and hence were not included in the subsequent analysis. Observations were interspersed between the phase calibrator (J0239–0234) and the target source, NGC 1068. Target scans were 6 min long, while phase calibrator scans were 2 min long. 3C286 and OQ208 were observed for flux density and bandpass calibration, respectively. The total time on target was ∼ 42 h across all epochs. Data were calibrated using the eMCP CASA pipeline version: v1.1.19 with CASA version: 5.8.0 (McMullin et al. 2007; Moldon 2021). Data from all epochs were self-calibrated and then divided into the respective 512 MHz bands for imaging to enhance the frequency sampling of the SED.

The *e*-MERLIN data were observed between 1.25 and 1.76 GHz, with central frequency at 1.5 GHz. Data were observed in three epochs in 2018 January 9, 10, and 12, under project ID CY6216,

Despite the challenges of measuring the radio–sub-mm wavelength SED of the AGN in NGC 1068, there is evidence that thermal free–free (FF) emission contributes significantly to the cm–sub-mm spectrum. Integrated over the source (component S1), the cm-wave spectrum is flat between ∼ 5 and ∼ 200 GHz (Gallimore et al. 1996; Muxlow et al. 1996; Inoue et al. 2020; Michiyama et al. 2023). The estimated brightness temperature at 5 GHz from VLBA observations is $T_B = 4 \times 10^6$ K, which is too low for synchrotron self-absorption (SSA) to be important in shaping the SED (Gallimore et al. 2004). The radio morphology of S1 roughly matches the warmest parts of the infrared (IR) emitting dusty torus and the distribution of water megamasers (Gámez Rosas et al. 2022). Thermal FF emission would imply the presence of a 10^6 K plasma intimately connected with dense molecular clouds traced by the masers and dust continuum (Gallimore et al. 2001, 2004; Gallimore & Impellizzeri 2023). This picture postulates a highly efficient plasma heating mechanism; the FF emission amounts to ∼20 per cent of the AGN bolometric luminosity (scaling from Gallimore et al. 2004), and for this reason, several authors have proposed alternative explanations (e.g. Inoue et al. 2020; Baskin & Laor 2021). The only way to settle this decades-long problem and to reveal the true nature of S1 is to construct a bona fide SED of the AGN of NGC 1068 to measure and separate the emission processes on parsec-scales. To accomplish this goal, we

Table 1. Observations and data used.

Frequency (GHz)	Obs' date	Interferometer	Project ID	Time (min)	Comments
1.25–1.76	2018 Jan 9–12	*e*-MERLIN	CY6216	1260	This work
4.5–7.5	2022 Mar–May	*e*-MERLIN	CY13006	3060	This work
8–12	2021 Jan 20,26	VLA	38677764	48	Archival (Mutie et al. 2024)
15	<1985 Nov 5	VLA	–	~ 195	Archival (Ulvestad, Neff & Wilson 1987)
18.5–23.5	2015 June–July	VLA	15A-345	180	Archival (Mutie et al. 2024)
93–106	2019 June 9	ALMA	2018.A.00038.S	26	Archival (Maeda et al. 2023)
241–257	2021 Sept 23	ALMA	2017.1.01666.S	60	Archival (Impellizzeri et al. 2019)
345–356	2017 Sept 8	ALMA	2016.1.00232.S	50	Archival (García-Burillo et al. 2019)
477–489	2022 Sept 8	ALMA	2021.1.00279.S	26	Archival (unpublished) (PI: Dieu Nguyen)
688–706	2015 Sept 25	ALMA	2013.1.00055.S	34	Archival (García-Burillo et al. 2016)

with 8 spws of 64 MHz width. The same calibration sources were used as in the 4.5–7.5 GHz observations above. The total observation time per epoch was 10 h 45 min, with scans interleaved between the target source and phase calibrator. Target scans were 7 min long, while phase calibrator scans were 3 min long. The total time on source target was ∼ 21 h.

All the ALMA data used in this work (see Table 1) were requested through the ALMA help desk. They used CASA pipeline version 6.5.4.9 to calibrate these data, then split the target source, averaged the data in time and frequency to minimize on storage and computing time while avoiding time and bandwidth smearing. These data were downloaded and inspected while flagging any obvious bad data (including any spectral lines). Clean data were self-calibrated and imaged per band. The details of reduction and imaging of the VLA data, 8−12 and 18.5−23.5 GHz, respectively, used in this work as summarized in Table 1 have been described in Mutie et al. (2024). The native angular resolution of VLA 8−12 GHz data is ∼ 0.15 arcsec with robust −2 of Briggs weighting. During the imaging and deconvolution we applied a *uv*-range of 15−3300 kλ and restoring beam was set to 0.06 arcsec (circular).

2.1 Imaging

Imaging procedures for all *e*-MERLIN 4.5–7.5 GHz and all VLA data (4–12 and 18–23 GHz) are detailed in Mutie et al. (2024). The *e*-MERLIN 1.25–1.76 GHz data were imaged in CASA task TCLEAN. In all ALMA data sets, imaging was performed in CASA with task TCLEAN. A multifrequency multiterm synthesis (mtmfs) deconvolver was used with a Taylor polynomial of 2. This was standardized for all data in this work. For the *e*-MERLIN 4.5–7.5 GHz, all the VLA, and ALMA data, the restoring beam and *uv*−range were matched at ∼0.06 arcsec and ∼15−3300 kλ (determined by the range of overlapping spatial scales available within these data sets), respectively, during imaging stage in CASA task TCLEAN. This ensures that all data sets used are sensitive to the same range of source spatial scales, and that source flux densities can be measured in the same physical regions.

2.2 Flux density measurements

Before extracting flux densities, astrometry checks were done in all data by overlaying the maps and comparing positions of compact sources by measuring the positions of their peak flux densities per beam and assuming the position of S1 as a prior. Flux density measurements of all components were then obtained by using the estimates file in CASA task IMFIT where the position of S1 was assumed as prior and beam size fixed at 60 mas in all measurements.

Table 2. Flux densities extracted by fitting 2D Gaussian from component S1. Similar CASA regions were used in all frequencies per component. The 1.4 and 15 GHz points are obtained from the literature and have a larger beam size hence are used as upper limits (UL) (Muxlow et al. 1996).

Frequency (GHz)	Interferometer	Flux (mJy)	rms (μJy beam⁻¹)
1.4 (UL)	*e*-MERLIN	<36.3±2.8	330
4.8	*e*-MERLIN	19.4±0.3	43
5.3	*e*-MERLIN	19.1±0.3	27
6.3	*e*-MERLIN	12.6±0.2	31
6.8	*e*-MERLIN	18.4±0.2	31
7.3	*e*-MERLIN	16.8±0.2	31
9.5	VLA	12.3±0.1	37
10.5	VLA	12.2±0.1	37
11.5	VLA	10.2±0.1	37
15 (UL)	VLA	<17±1	–
18.9	VLA	13±0.1	23
19.4	VLA	12.6±0.1	23
19.9	VLA	12.5±0.1	37
21.9	VLA	12.1±0.1	53
22.3	VLA	12.5±0.1	54
22.9	VLA	12±0.1	52
94	ALMA	11±0.6	24
100	ALMA	10.2±0.5	24
241	ALMA	10.6±0.6	24
256	ALMA	9.9±0.1	24
345	ALMA	16.1±0.3	87
357	ALMA	13.9±0.1	87
477	ALMA	18.7±0.5	170
483	ALMA	19.6±0.4	170
688	ALMA	20.0±2.5	80
697	ALMA	17.0±1.7	80
706	ALMA	16.5±1.9	75

The flux densities obtained for each observed frequency are presented in Table 2, together with the statistical errors. To account for possible systematic uncertainties in the absolute flux calibrations of the different observatories, we added a systematic error of 10 per cent in quadrature in all flux density errors.

3 SED MODELLING

We have a set of continuum flux densities obtained at a consistent angular resolution and *uv*-coverage in the AGN (region S1). In addition, we include data from observations with a poorer angular resolution as hard upper limits to the SED, as they encapsulate more diffuse emission; we leave a 1σ margin to be conservative with the strict limits adopted. We introduce a robust SED fitting scheme to derive physical information from the measured continuum SED. Here

we present a summary of the model that has been used in the study of other RQ AGNs (Shablovinskaya et al. 2024), and leave further details to be presented in del Palacio et al. (in preparation).

In general, the SED of an RQ galaxy consists of multiple components, including a diffuse population of cosmic ray electrons, diffuse ionized gas, dust, and possibly a very compact synchrotron source in the core of the AGN dubbed the corona (e.g. Panessa et al. 2019). The total emission from the model is the sum of these components. In addition, absorption by ionized gas can affect the emission at low frequencies. We parametrize these components as detailed below, adopting a reference frequency of $\nu_0 = 100$ GHz. To deal with a large parameter space, we fit the SED using the standard sampler for Markov Chain Monte Carlo EMCEE (Foreman-Mackey et al. 2013) implemented in the Python package Bilby (Ashton et al. 2019). We assume flat priors over a wide range of values for all fitted model parameters.

3.1 Synchrotron from diffuse cosmic ray electrons

Diffuse cosmic ray electrons emit an optically thin synchrotron SED with a steep spectral index $\alpha_{sy} \leq -0.5$. We write this as

$$S_{sy}(\nu) = A_{sy} \left(\frac{\nu}{\nu_0} \right)^{\alpha_{sy}}, \tag{1}$$

where $S_{sy}(\nu)$ is the synchrotron spectrum at a given frequency (ν) and A_{sy} is a normalization constant. These electrons can be related either to a jet or star formation.

3.2 FF emission from ionized gas

The ionized gas emits FF radiation with an intrinsic spectral index of $\alpha = -0.1$ where it is optically thin, such that

$$S_{ff}(\nu) = A_{ff} \left(\frac{\nu}{\nu_0} \right)^{-0.1}, \tag{2}$$

where A_{ff} is a normalization constant. We note that at low frequencies this emission can drop as the medium becomes optically thick ($\alpha = 2$ instead of -0.1). However, this effect is unlikely to be relevant considering that the low-frequency (<5 GHz) SED can be dominated by synchrotron emission and/or FF absorption (FFA). We thus refrain from including this opacity effect in the model to keep the number of free parameters to a minimum.

3.2.1 FFA by diffuse gas

The SED can be significantly affected at low frequencies due to FFA by ionized gas. For simplicity, we assume a diffuse, homogeneous medium but the effects of a clumpy medium can be relatively similar though including additional free parameters and are not likely to be constrained without observations at $\nu < 1$ GHz (e.g. Lacki 2013; Ramírez-Olivencia et al. 2022). We thus introduce only one free parameter, namely the frequency at which the diffuse gas becomes optically thick, ν_{diff}. The absorption-corrected emission is ,

$$S_{sy,abs}(\nu) = S_{sy,int} e^{-\tau_{diff}}, \tag{3}$$

where $S_{sy,int}$ is the intrinsic synchrotron spectrum and $\tau_{diff} = (\nu/\nu_{diff})^{-2.1}$.

3.3 Synchrotron emission from a compact corona

The corona is a very compact region close to the accreting SMBH that is filled with extremely hot plasma. Inoue & Doi (2014) proposed that

if non-thermal electrons coexist in the corona, they would interact with the strong magnetic fields and generate synchrotron emission. This synchrotron radiation would be optically thick (due to SSA) at radio-cm frequencies, making it extremely challenging to detect, but it would be optically thin in the high-frequency end (mm–sub-mm regime), hence detectable by sensitive instruments such as ALMA.

Recent works analysing the mm continuum emission from a compact core in AGNs have provided strong support for this idea (Behar et al. 2015, 2018; Kawamuro at al. 2022; Ricci at al. 2023; Shablovinskaya et al. 2024). The synchrotron SED of a compact source as a corona is shaped by SSA at frequencies below ν_{SSA} (Inoue & Doi 2014). The SED is a power law with a negative spectral index $\alpha \sim -0.5$ to -1 at frequencies above ν_{SSA}, whereas it has a positive spectral index of $\alpha = 2.5$ below ν_{SSA}. The value of ν_{SSA} and the overall corona SED depend on the properties of the corona (magnetic field, size) and the relativistic electrons there. We thus adopt a physical model to compute this SED self-consistently. The first application of this model was already presented in Shablovinskaya et al. (2024). In short, the model is based on that of the hybrid corona by Inoue & Doi (2018), implemented by adapting the code from Margalit & Quataert (2021) for synchrotron emission by a hybrid plasma. We parametrize the radius of the corona as $R_c = r_c R_g$, where r_c is an adimensional parameter, $R_g \propto M_{BH}$ is the gravitational radius, and we adopt an SMBH mass of $M_{BH} = 1.66 \times 10^7$ M$_\odot$ (Gallimore et al. 2024). To reduce the number of free parameters, we tie the magnetic field strength to the non-thermal electron population by adopting a scaling between the energy density in the magnetic fields (U_B) and in non-thermal electrons ($U_{nt,e}$), namely $\eta_B = U_B/U_{nt,e} = 40$. We then allow the parameters r_c and $\delta = U_{nt,e}/U_{th,e}$ (fraction of the energy in non-thermal electrons w.r.t. thermal electrons) to vary, while we fix the temperature and Thompson opacity of the corona, $kT = 166$ keV and $\tau_T = 0.25$, respectively, and the spectral index of the non-thermal electron energy distribution, $p = 2.7$. We note that the choice of these last parameters has only a small effect on the SED (del Palacio et al. in preparation).

3.4 Thermal emission from dust

Dust emission is modelled as a modified-blackbody spectrum. This is characterized by the frequency ν_{τ_1} at which the dust opacity becomes equal to unity, and the index β of the opacity coefficient $\kappa_\nu \propto \nu^\beta$ (with $\beta \approx 1$–2); at $\nu < \nu_{\tau_1}$ the SED is optically thin and has a spectral index $\alpha = 2 + \beta$, while at $\nu > \nu_{\tau_1}$ it is optically thick and $\alpha = 2$. This can be parametrized as

$$S_d(\nu) = A_d \left(\frac{\nu}{\nu_0} \right)^2 \left(1 - e^{-\tau_d} \right), \tag{4}$$

where S_d is the dust spectrum, A_d is a normalization constant, and $\tau_d = (\nu/\nu_{\tau_1})^\beta$. Given the lack of sufficient sub-mm and far-IR data to fit the dust component, we simply fix $\beta = 2$ and $\nu_{\tau_1} = 800$ GHz, and constrain only the normalization A_d. We note that the values adopted for β and ν_{τ_1} have no impact on the results obtained with the current data set.

4 RESULTS AND DISCUSSION

In this section, we fit different physically motivated models to the data. First, we fit FFA from diffuse gas and a simple power-law model to the data whose results (spectral index) show consistency with the thermal FF spectrum, hence we consider this a thermal FF model as discussed in Section 4.1.1. The fit shows that some components are
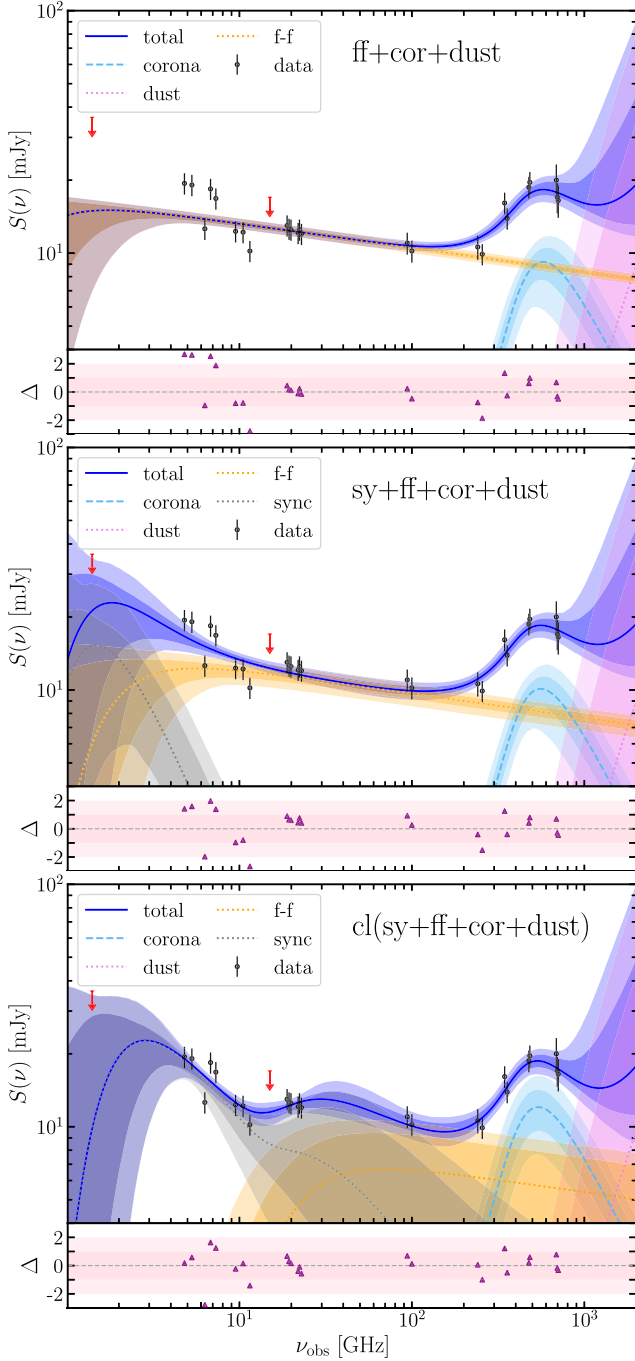
Figure 2. SED fitting of the S1 source (AGN) in NGC 1068 for the different model assumptions detailed in Section 4.1. The shaded regions represent the 1σ and 2σ confidence intervals. The bottom sub-panels show the residuals of the fit (($S_{obs} - S_{model}$)/$S_{obs,error}$).

missing, especially on the higher end of the spectrum (>200 GHz). We then add a corona and dust model motivated by works of Inoue et al. (2020), Michiyama et al. (2023), and García-Burillo et al. (2016). This model fits well, but the dust component is unconstrained at all as reported in García-Burillo et al. (2016), and instead, all the data points seemed to fit the corona bump well as shown in Fig. 2 top panel. We then add a synchrotron model as presented in Section 4.1.2 to fit the lower end of the spectrum <10 GHz as shown in Fig. 2 middle panel. This fits well but leaves a kink between 10 and

100 GHz. We then add a clumpy absorption model (Section 4.1.3) to take care of the kink as shown in Fig. 2 bottom panel.

In Fig. 2 we present the SED of the AGN of NGC 1068 (S1) and our model fittings under the above-mentioned different assumptions. In very simplified terms, the SED is potentially dominated by diffuse synchrotron at frequencies $\lesssim$2 GHz, FF between $\sim$2 and 200 GHz, the corona between $\sim$200 and 700 GHz, and most likely dust at higher frequencies (although only a UL is derived with the current data set). In addition, the impact of FFA might become relevant at frequencies below $\sim$2 GHz. In this section, we provide a more comprehensive discussion of the SED. In the text, we round some numbers and error bars to simplify the discussion and present the corner plot with the complete details of the posteriors of the fit in Appendix A.

4.1 The SED below 200 GHz

It is currently challenging to determine whether the SED is significantly absorbed below 4 GHz, as we lack data below $\sim$2 GHz with the required high angular resolution and sensitivity to unambiguously detect and separate S1/AGN from the surrounding emission. (Table 2). However, the $\sim$ 0.016 arcsec angular resolution VLBA observations at 1.7 and 1.4 GHz by Roy et al. (1998) and Gallimore et al. (2004), respectively, did not detect component S1 and placed upper limits of $\sim$0.06 mJy. If we include this upper limit, the SED would become strongly absorbed at frequencies $\lesssim$2 GHz, likely due to FFA in a diffuse medium (e.g Inoue et al. 2020; Michiyama et al. 2023). The VLBA however detects S1 at frequencies above $\sim$5 GHz (e.g Roy et al. 1998; Gallimore et al. 2004). Similar conclusions were reached for 3C 84, for which VLBA observations at 5 GHz failed to detect the counter jet of its *one-sided* jet, but observations at 15 and 22 GHz did detect it, which was interpreted as FFA due to an absorbing screen in front of the counter jet (Vermeulen, Readhead & Backer 1994; Walker, Romney & Benson 1994).

However, taking into account the lack of sufficient short spacings in these VLBA observations (with the shortest baseline between Los Alamos and Pie Town at 236 km), we can infer that most of the flux is either resolved out and unrecovered in the VLBA observations. Alternatively, there could be strong FFA. The *e*-MERLIN 1.4 GHz data have an angular resolution of $\sim$ 0.19 arcsec and do not adequately separate the emission from the AGN from the surrounding components to enable a reliable flux density to be determined. It is a challenge to combine these data with the VLBA data, since *e*-MERLIN's longest baseline (217 km) and VLBA's shortest baseline (236 km) do not overlap. We used CASA task IMFIT and fixed some parameters such as the position of the peak flux (guided by the *e*-MERLIN 4.5–7.5 GHz map), major and minor axes, and the position angle to extract flux densities that we used as upper limits from *e*-MERLIN 1.4 GHz data.

At higher angular resolutions, the source S1 is detected with the VLBA at 5 and 8.4 GHz (measuring 9.1±0.8 and 5.4±0.5 mJy, respectively), and showing a high brightness temperature $T_B \approx 4 \times 10^6$ K and a relatively flat spectrum $\alpha \approx -0.17$ (Gallimore et al. 2004). More recent VLBA observations at 22 GHz with the High Sensitivity Array show a compact but structured source with a flux density of 7 ± 1 mJy (Gallimore et al. 2024). This suggests that the emission from S1 on sub-pc scales does not become steeper at higher frequencies. For reference, we show the SED between 1 and 30 GHz including these VLBA data in Fig. 3 for comparison with our data. We highlight that our observations have an angular resolution of $\sim$ 0.06 arcsec $\approx$ 4 pc (which includes the BLR and the dusty torus), whereas VLBA observations, with an angular resolution of $\sim$ 0.01 arcsec $\approx$ 1 pc, probe $\lesssim$ pc scales. It is therefore unclear at this
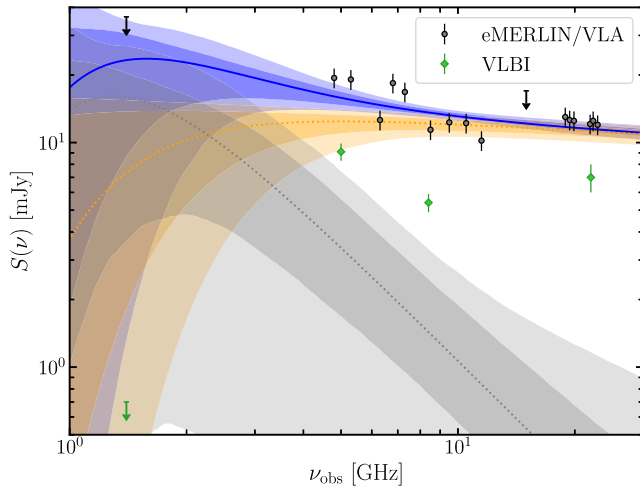
Figure 3. Same as the middle panel of Fig. 2, but limited to the radio-cm range. We also show in green diamonds the flux densities from VLBA measurements in the literature. The *e*-MERLIN and VLA data probe consistent angular scales of ≈ 60 mas, whereas the VLBA data are only sensitive to $\lesssim 10$ mas.

stage whether the radio-cm emission seen on scales $\lesssim 0.01$ arcsec is produced by hot ionized gas associated with the AGN, or non-thermal emission from an unresolved jet that is partially synchrotron self-absorbed. However, we can already conclude from Fig. 3 that a significant fraction (if not most) of the emission that we detect on scales of ~ 0.06 arcsec is filtered out on VLBA observations, and thus produced on relatively larger scales.

Next, we describe various SED fittings under different assumptions, concluding that the favoured SED is the one shown in Fig. 2 middle panel. In all cases, we include the diffuse FFA described in Section 3.2.1. We also note that the corona and dust components do not change significantly between the models, as they (indirectly) depend only slightly on the SED at $\nu < 200$ GHz.

4.1.1 FF + corona + dust

We use the model described in Section 3 but assume that there is no diffuse synchrotron emission. We show the fitted SED in the top panel of Fig. 2. The model can reproduce adequately most of the SED ($\chi^2_{\rm red} = 2.1$), but the residuals of the fit are quite high between 5 and 8 GHz, suggesting that this model is incomplete.

To rule out other possibilities, we also fit the low-frequency SED using a general phenomenological power-law component with an arbitrary spectral index between -2 and 1. This component could mimic, for example, the synchrotron emission from the compact radio jet (a partially optically thick synchrotron source). The fit yields $\alpha = -0.15 \pm 0.03$, which is consistent with FF emission ($\alpha = -0.1$), as reported in Muxlow et al. (1996), Gallimore et al. (1996), and Gallimore et al. (2004).

4.1.2 Synchrotron + FF + corona + dust

The SED of NGC 1068 at $\nu \lesssim 3$ GHz can be dominated by optically thin diffuse synchrotron emission, although FFA may also be relevant below ~ 2 GHz. The SED fit presented in the middle panel of Fig. 2 is slightly better than without the synchrotron component ($\chi^2_{\rm red} = 1.8$), and is therefore the preferred one. However, the fit shows a strong degeneracy between the spectral index of the synchrotron emission,
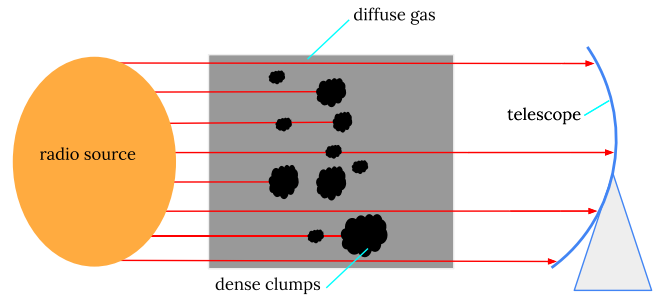
Figure 4. A schematic of the clumpy absorbing medium along the line of sight, amid a diffuse absorbing gas. The clumps become optically thick at a frequency $\nu_{\rm cl}$, resulting in absorption of a fraction $f_{\rm cov}$ of the total emission (Section 4.1.3).

which hits the hard limit of -2 imposed in the priors, the intensity of the synchrotron emission, and the value of $\nu_{\rm diff}$ (Fig. A2). We cannot draw strong conclusions about the low-frequency (< 5 GHz) part of the SED given the lack of data in this range, and the difficulty of spatially separating emission from S1 and adjacent radio emission within the region. The upper limit at 1.4 GHz gives only a loose constraint to these parameters but is insufficient to fully characterize the SED.

4.1.3 Clumpy absorption + synchrotron + FF + corona + dust

There seems to be a small decrease in flux densities between 10 and 20 GHz that, if real, the previous models cannot reproduce. For this reason, we decided to explore under which conditions a model could account for this behaviour. Following e.g. Lacki (2013), we assume that the ionized medium is inhomogeneous and clumpy. The FFA absorption depends on the opacity and distribution of the clumps. The clumps can efficiently absorb the synchrotron emission, but also part of the emission propagates between the less dense inter-clump medium, remaining unaffected or with different absorption characteristics (e.g. Lacki 2013; Ramírez-Olivencia et al. 2022). A sketch of this scenario is shown in Fig. 4. This absorption can be modelled in terms of two parameters: the frequency at which the clumps become optically thick, $\nu_{\rm cl}$, and the covering factor of the medium, $f_{\rm cov}$ (e.g. Conway, Elitzur & Parra 2018, for a similar approach). In such a case, one can parametrize the absorption-corrected emission as

$$S_{\rm sy,abs}(\nu) = S_{\rm sy,int} \left[1 - f_{\rm cov} \left(1 - e^{-\tau_{\rm cl}} \right) \right], \tag{5}$$

where $S_{\rm sy,int}$ is the intrinsic synchrotron spectrum and $\tau_{\rm cl} = (\nu/\nu_{\rm cl})^{-2.1}$. Furthermore, the more diluted gas in-between clumps can contribute with an additional absorption factor $e^{-\tau_{\rm diff}}$, with $\nu_{\rm diff} < \nu_{\rm cl}$ the frequency at which the diffuse medium becomes optically thick (same as Section 3.2.1). We further assume that the FF emission (Section 3.2) also becomes optically thick at $\nu = \nu_{\rm cl}$.

The bottom panel of Fig. 2 shows the SED fit using this model ($\chi^2_{\rm red} = 1.2$). We obtain $\nu_{\rm cl} \approx 20$ GHz and $f_{\rm cov} \sim 54$ per cent. Radio sources with turn-over frequencies >5 GHz have been reported in several works (Clemens et al. 2010; O'Dea & Saikia 2021; Ballieux et al. 2024). In Clemens et al. (2010), they attributed the high turn-over frequencies to H II regions with high densities of ionized gas from rising star formation rates in those sources. In this work, the requirement of $\nu_{\rm cl} \sim 20$ GHz would require either even higher densities, beyond those found in the so-called hyper-compact H II regions (Yang et al. 2021, and references therein), or larger sizes of the ionized regions. We analyse this in more detail below.

4.1.4 High densities?

We can estimate the density at which $\tau_{cl} = 1$ from the condition (e.g. using equation 1 in Yang et al. 2021):

$$\left(\frac{v_{cl}}{\text{GHz}}\right)^{2.1} = 0.082 \left(\frac{T_e}{\text{K}}\right)^{-1.35} \left(\frac{n_e^2 D}{\text{cm}^{-6}\,\text{pc}}\right), \qquad (6)$$

where D is the characteristic linear size of the ionized region (assuming it is roughly isotropic), and T_e and n_e are the temperature and number density of the electrons, respectively. For simplicity, we fix the electron temperature to the canonical value of 10^4 K, and we substitute $v_{cl} = 20$ GHz. This leads to

$$\left(\frac{n_e}{\text{cm}^{-3}}\right)^2 \left(\frac{D}{\text{pc}}\right) = 1.65 \times 10^9. \qquad (7)$$

Assuming a characteristic size similar to that of the angular resolution of our observations, i.e. $D \sim 2$ pc, equation (7) yields a density of $n_e \sim 3 \times 10^4$ cm^{-3}. We note that this corresponds to a column density consistent with the low end of those inferred from spectral modelling of the X-ray SED ($N_H \approx 10^{23}$–10^{25} cm^{-2}; Bauer et al. 2015). Alternatively, adopting a size similar to BLR clouds, i.e. $D \sim 10^{-5}$ pc, we get a density of $n_e \sim 10^7$ cm^{-3}, which is about ~ 1 per cent of the gas in a typical BLR cloud (e.g. Netzer 2015, and references therein). We conclude that, in principle, the conditions required for FFA to produce a spectral change between 10 and 20 GHz seem feasible. However, we cannot rule out other possibilities as well.

4.1.5 Is component S1/AGN variable?

An alternative plausible explanation for the scatter in the data points between ~ 5 and 20 GHz could be source variability. Based on causality arguments, variability on time-scales of ~ 7 yr (the time the 8–12 and 18–23 GHz observations were used in this study) implies an emission region of size ≤ 2 pc. This size is consistent with VLBA observations (Greenhill & Gwinn 1997; Roy et al. 1998; Gallimore et al. 2004), which measure the size of S1 to be ~ 2 pc in diameter. The flux densities measured at 5 GHz with the *e*-MERLIN between 1992, 2018, and 2023 (this work) are 12±2, 15.2±1.2, and 19.1±0.3 mJy, respectively, while the flux densities measured at ~ 20 GHz by the VLA between 1992 and 2015 are 19 and 12.5±0.1 mJy, respectively (Mutie et al. 2024). We note that there may be minor differences between 1992 and later data points due to differing uv-coverages of data sets and any flux density scaling difference between the early narrow-band VLA and MERLIN and later wideband VLA and *e*-MERLIN observations. However, both 2015 and later data points have been measured using similar procedures (as detailed in Mutie et al. 2024, and in this work). The VLA 43 GHz observations conducted between 2000 (Cotton et al. 2008) and 2019 (Cotton et al. in preparation) reveal a decrease in the flux densities of S1 from 13.1±0.4 to 10.4±0.1 mJy, further supporting the variability of S1. Based on these findings, we conclude that source variability is likely to occur in NGC 1068. This variability is consistent with the AGN variability levels of ±10–20 per cent reported in other local Seyfert galaxies (see Mundell et al. 2003; Jones et al. 2011; Williams et al. 2017, and references therein).

4.2 SED between ~200 and 706 GHz: the corona

The flux density of S1 increases between ~ 200 and ~ 500 GHz and flattens (or even decreases slightly) from ~ 500 to ~ 706 GHz. The initial model fits by Inoue et al. (2020) and Michiyama et al. (2023) favour the presence of synchrotron emission from a compact

corona to explain this part of the SED. However, they used data of varied angular resolutions and the effect of it is evident in Fig. 3 where VLBA fluxes are significantly below *e*-MERLIN and VLA at similar frequencies. The SED shape in the sub-mm rules out that this emission is produced by dust, which has $\alpha > 2$ (Section 3.4); trying to fit an SED without the inclusion of a coronal component leads to a very large $\chi^2_{red} = 4.2$ (compared with $\chi^2_{red} = 1.8$ with a corona component component fitted as discussed in Section 4.1.2) regardless of the values of β and v_{τ_1}. This result appears to contradict the previous interpretation, which assumed a different dust model to explain the sub-mm flux density and was based upon less well-sampled SED data (García-Burillo et al. 2016; Michiyama et al. 2023).

We adopt flat priors for the corona parameters r_c and $\log \delta$ in the ranges (20,200) and (−3, 0), respectively. Our SED fitting suggests that the corona component dominates the SED between 400 and 800 GHz, with a peak at ≈ 550 GHz (Fig. 2). The corresponding coronal parameters from the model in Section 4.1.2 are $r_c = 70 \pm 5$ and $\log \delta = -1.01 \pm 0.10$ ($\delta \approx 0.09$), corresponding to $B \approx 148$ G. Depending on the model assumptions (Section 4.1), these values can have an additional ~ 10 per cent dispersion (Appendix A). Our results are consistent with those obtained by Inoue et al. (2020), considering that they derived $r_c = 20$ assuming $M_{BH} = 5 \times 10^7$ M$_\odot$ (which would correspond to $r_c \approx 60$ for the more updated value we adopt of $M_{BH} = 1.66 \times 10^7$ M$_\odot$) and fixing $\delta = 0.03$. The size of the corona corresponds to $R_c \approx 0.07$ light day (ld), which suggests that its emission can be variable on time-scales of ~ 2 h (Shablovinskaya et al. 2024). The dust component is very poorly constrained, with essentially only a loose upper limit derived, because of the lack of high angular resolution observations at higher frequencies (in particular, in the far-IR).

We can put our results in the context of the mm and X-ray luminosity correlations found by Kawamuro at al. (2022) and Ricci at al. (2023). From our SED fitting, we can extract the total mm luminosity at the required frequency and use it to calculate the expected X-ray luminosity; we can then compare this value with that derived from X-ray observations. To accomplish this, we first derived the hard X-ray (unabsorbed) luminosity in the 14–150 keV range using as a reference the intrinsic X-ray luminosity in the 10–40 keV energy range inferred from observations, $L_{10-40\,\text{keV}} \approx 1.5 \times 10^{43}$ erg s^{-1}, and the spectral index, $\Gamma = 2.10 \pm 0.07$ (Bauer et al. 2015). We obtain $L_{14-150\,\text{keV}} = (8.6 \pm 1.3) \times 10^{42}$ erg s^{-1} assuming a 10 per cent error on the 10–40 keV luminosity. If we take the luminosity at 230 GHz from our model fitting and use it in the prescription between the 230 GHz luminosity and the 14–150 keV luminosity from Kawamuro at al. (2022) (their table 2 for RQ AGNs), we obtain $L_{14-150\,\text{keV}} \approx 2.2 \times 10^{43}$ erg s^{-1}. Similarly, using the 100 GHz luminosity from our model and the correlation from equation (1) in Ricci et al. (2023), we obtain $L_{14-150\,\text{keV}} \approx 1.9 \times 10^{43}$ erg s^{-1}. The rough agreement between the inferred values from the correlation and the observations is remarkable considering that our observations at ~ 100–~ 250 GHz will include significant levels of emission not arising from the corona (Fig. 2), which might explain why the X-ray luminosity is overpredicted by a factor of $\gtrsim 2$.

5 SUMMARY AND CONCLUSIONS

We used radio–sub-mm data between ~ 5 and 700 GHz, matched in angular resolution at ~ 0.06 arcsec and uv-coverage to probe regions of ~ 2 pc radius around the SMBH. Our work improves on those from Inoue et al. (2020) and Michiyama et al. (2023) in that they used data of different angular resolutions. The SED of S1

shows a prominent bump between 200 and 700 GHz, consistent with synchrotron radiation from a compact corona with radius $R_c \approx 70 \pm 5\, R_g$, a non-thermal electron population with a fraction of ~ 10 per cent of the energy density of the thermal electrons, and magnetic field strength of $B \approx 148$ G. The SED of the AGN (S1) is dominated by FF emission below ≈ 200 GHz, with some poorly constrained levels of synchrotron emission possibly relevant below 3 GHz. There is a hint of a diffuse FF absorbing medium relevant at frequencies below 2 GHz. The kink in the SED around 10–20 GHz could be either due to intrinsic variability of the source or to a clumpy and high-density absorbing medium.

Future observations at frequencies < 2 GHz are crucial to further constrain the SED, allowing better characterization of the FF absorbing diffuse medium and the spectral index of the diffuse synchrotron emission. Such observations are possible with EVN + *e*-MERLIN at 1.4 GHz and with the international LOFAR telescope at ~ 200 MHz, which can provide matched angular resolution and uv-coverage to this work. ALMA Band 10 (787–950 GHz) data could also provide important constraints on dust emission. In a follow-up paper, we will investigate in detail the broad-band SED of the whole nuclear region of NGC 1068, i.e components NE, C, S2, and S3 (see Fig. 1), providing the conditions of the jet components as well.

ACKNOWLEDGEMENTS

DATA AVAILABILITY

The data on which this paper is based are publicly available from the *e*-MERLIN, VLA, and ALMA archives under the project IDs described in Table 1. Calibrated image products are available upon reasonable request to the corresponding author.

REFERENCES

Aartsen M. et al., 2020, Phys. Rev. Lett., 124, 051103
Antonucci R., 1993, ARA&A, 31, 473
Antonucci R. R. J., Miller J. S., 1985, ApJ, 297, 621
Ashton G. et al., 2019, ApJS, 241, 27

Ballieux F. J., Callingham J. R., Röttgering H. J. A., Slob M. M., 2024, A&A, 689, A264
Baskin A., Laor A., 2021, MNRAS, 508, 680
Bauer F. E. et al., 2015, ApJ, 812, 116
Behar E., Baldi R. D., Laor A., Horesh A., Stevens J., Tzioumis T., 2015, MNRAS, 451, 517
Behar E., Vogel S., Baldi R. D., Smith K. L., Mushotzky R. F., 2018, MNRAS, 478, 399
Bland-Hawthorn J., Lumsden S. L., Voit G. M., Cecil G. N., Weisheit J. C., 1997, Ap&SS, 248, 177
Capetti A., Macchetto F., Axon D. J., Sparks W. B., Boksenberg A., 1995, ApJ, 452, L87
Capetti A., Robinson A., Baldi R. D., Buttiglione S., Axon D. J., Celotti A., Chiaberge M., 2013, A&A, 551, A55
Clemens M. S., Scaife A., Vega O., Bressan A., 2010, MNRAS, 405, 887
Conway J. E., Elitzur M., Parra R., 2018, ApJ, 865, 70
Cotton W. D., Jaffe W., Perrin G., Woillez J., 2008, A&A, 477, 517
Eichmann B., Oikonomou F., Salvatore S., Dettmar R.-J., Tjus J. B., 2022, ApJ, 939, 43
Foreman-Mackey D., Hogg D. W., Lang D., Goodman J., 2013, PASP, 125, 306
Gallimore J. F., Impellizzeri C. M. V., 2023, ApJ, 951, 109
Gallimore J. F., Baum S. A., O'Dea C. P., Pedlar A., 1996, ApJ, 458, 136
Gallimore J. F., Henkel C., Baum S. A., Glass I. S., Claussen M. J., Prieto M. A., Von Kap-herr A., 2001, ApJ, 556, 694
Gallimore J. F., Baum S. A., O'Dea C. P., 2004, ApJ, 613, 794
Gallimore J. F., Impellizzeri C. M. V., Aghelpasand S., Gao F., Hostetter V., Lankhaar B., 2024, ApJ, 975, L9
Gámez Rosas V. et al., 2022, Nature, 602, 403
García-Burillo S. et al., 2016, ApJ, 823, L12
García-Burillo S. et al., 2019, A&A, 632, A61
GRAVITY Collaboration, 2020, A&A, 634, A1
Greenhill L. J., Gwinn C. R., 1997, Ap&SS, 248, 261
Imanishi M., Nakanishi K., Izumi T., 2016, ApJ, 822, L10
Imanishi M., Nakanishi K., Izumi T., Wada K., 2018, ApJ, 853, L25
Impellizzeri C. M. V. et al., 2019, ApJ, 884, L28
Inoue Y., Doi A., 2014, PASJ, 66, L8
Inoue Y., Doi A., 2018, ApJ, 869, 114
Inoue Y., Khangulyan D., Inoue S., Doi A., 2019, ApJ, 880, 40
Inoue Y., Khangulyan D., Doi A., 2020, ApJ, 891, L33
Jones S., McHardy I., Moss D., Seymour N., Breedt E., Uttley P., Körding E., Tudose V., 2011, MNRAS, 412, 2641
Kawamuro et al., 2022, ApJ, 938, 87
Krips M., Eckart A., Neri R., Schödel R., Leon S., Downes D., García-Burillo S., Combes F., 2006, A&A, 446, 113
Lacki B. C., 2013, MNRAS, 431, 3003
Maeda K. et al., 2023, ApJ, 942, 17
Margalit B., Quataert E., 2021, ApJ, 923, L14
Marinucci A. et al., 2016, MNRAS, 456, L94
Mason R. E., Geballe T. R., Packham C., Levenson N. A., Elitzur M., Fisher R. S., Perlman E., 2006, ApJ, 640, 612
McMullin J. P., Waters B., Schiebel D., Young W., Golap K., 2007, in Shaw R. A., Hill F., Bell D. J.eds, ASP Conf. Ser. Vol. 376, Astronomical Data Analysis Software and Systems XVI. Astron. Soc. Pac., San Francisco, p. 127
Michiyama T., Inoue Y., Doi A., 2023, PASJ, 75, 874
Moldon J., 2021, Astrophysics Source Code Library, record ascl:2109.006
Mundell C. G., Wrobel J. M., Pedlar A., Gallimore J. F., 2003, ApJ, 583, 192
Mutie I. M. et al., 2024, MNRAS, 527, 11756
Muxlow et al., 1996, MNRAS, 278, 854
Netzer H., 2015, ARA&A, 53, 365
O'Dea C. P., Saikia D. J., 2021, A&AR, 29, 3
Padovani P. et al., 2024, Nat. Astron., 8, 1077
Panessa F., Baldi R. D., Laor A., Padovani P., Behar E., McHardy I., 2019, Nat. Astron., 3, 387
Ramírez-Olivencia N., Varenius E., Pérez-Torres M., Alberdi A., Conway J. E., Alonso-Herrero A., Pereira-Santaella M., Herrero-Illana R., 2022, A&A, 658, A4

Ramos Almeida C., Ricci C., 2017, Nat. Astron., 1, 679

Ricci et al., 2023, ApJ, 952, L28

Roy A. L., Colbert E. J. M., Wilson A. S., Ulvestad J. S., 1998, ApJ, 504, 147

Shablovinskaya et al., 2024, A&A, 690, A232

Tully R. B., 1988, Nearby galaxies catalog, Cambridge University Press, Cambridge, (Provided by the SAO/NASA Astrophysics Data System), https://ui.adsabs.harvard.edu/abs/1988ngc..book.....T

Ulvestad J. S., Wilson A. S., 1989, ApJ, 343, 659

Ulvestad J. S., Neff S. G., Wilson A. S., 1987, AJ, 93, 22

Vermeulen R. C., Readhead A. C. S., Backer D. C., 1994, ApJ, 430, L41

Walker R. C., Romney J. D., Benson J. M., 1994, ApJ, 430, L45

Williams D. et al., 2017, MNRAS, 472, 3842

Yang A. Y. et al., 2021, A&A, 645, A110

Young A. J., Wilson A. S., Shopbell P. L., 2001, ApJ, 556, 6

APPENDIX A: POSTERIOR DISTRIBUTION

In Figs A1–A3 we present the posterior distributions of the fitted parameters for S1 in Section 4.1. The top panels of each plot show the 1D distributions of each parameter. The plots are obtained by the MCMC fitting described in Section 3.

We focus on Fig. A2, the cornerplot for the preferred model (Section 4.1.2). Despite the broad-band coverage of our data, significant degeneracies between the parameters persist, especially for the synchrotron and FFA components, which are relevant at low frequencies where only an upper limit at 1.4 GHz is available. We note that the parameter $\alpha_{\rm sy}$ hits the hard limit at -2 imposed in the priors, as a steeper synchrotron spectrum is most likely unphysical.
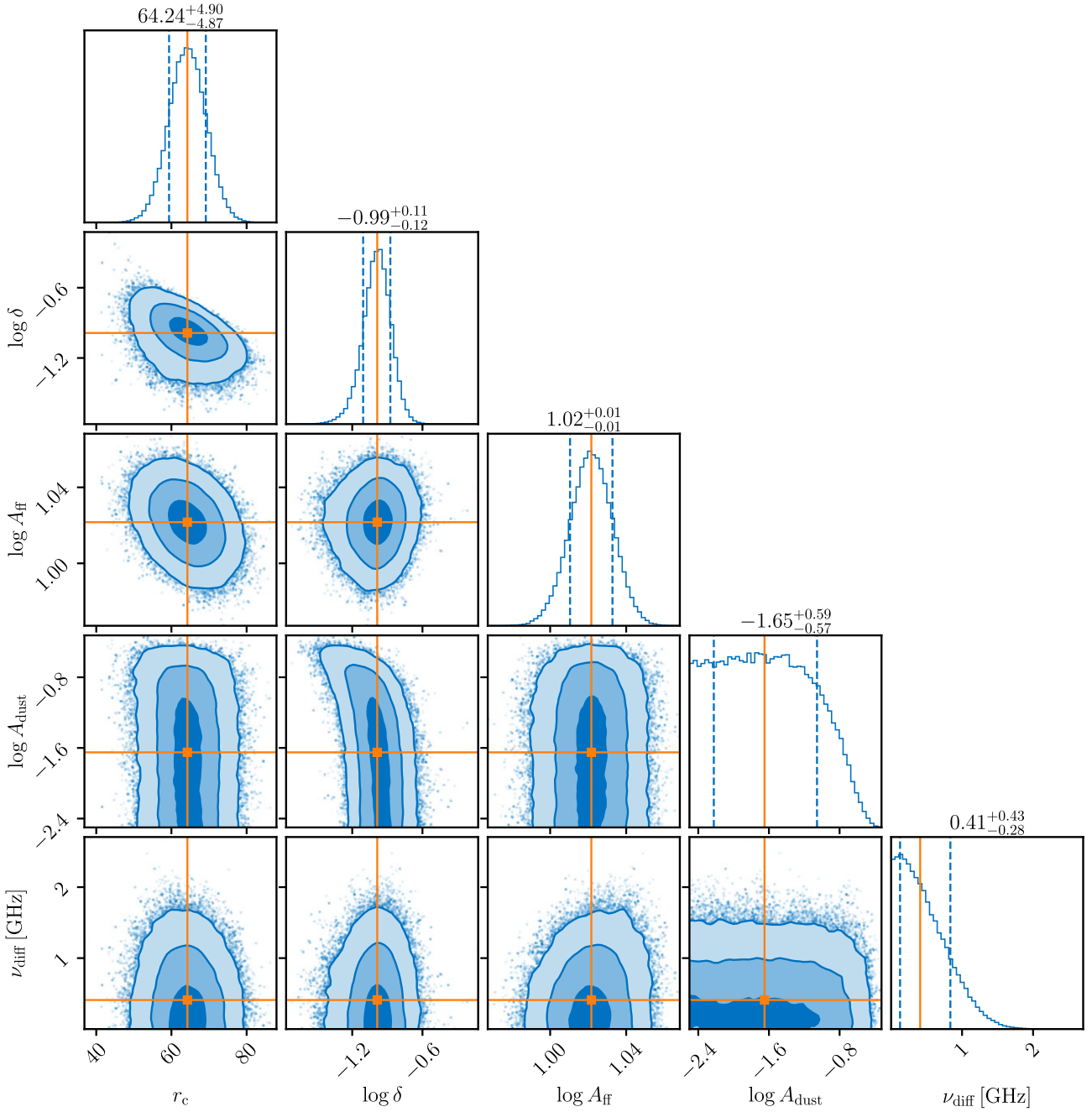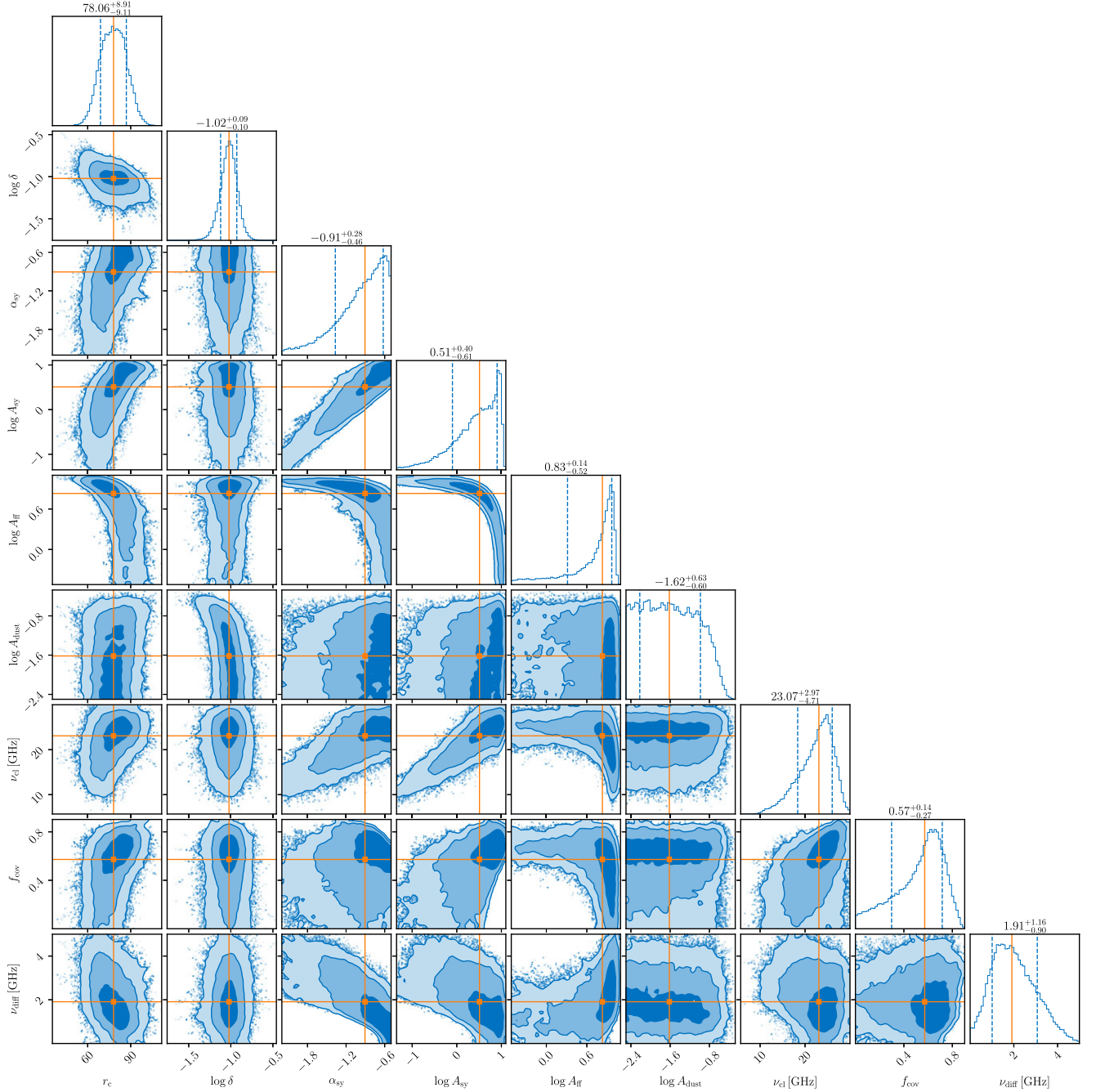
Figure A1. Posteriors of the MCMC fitting in Section 4.1.1 (fit shown in Fig. 2, top panel). The top panels show the 1D distributions of each parameter, with the orange line marking the position of the median, and the dashed lines the 1σ confidence interval. We note that for $\log A_{\mathrm{dust}}$ only an upper limit is established.
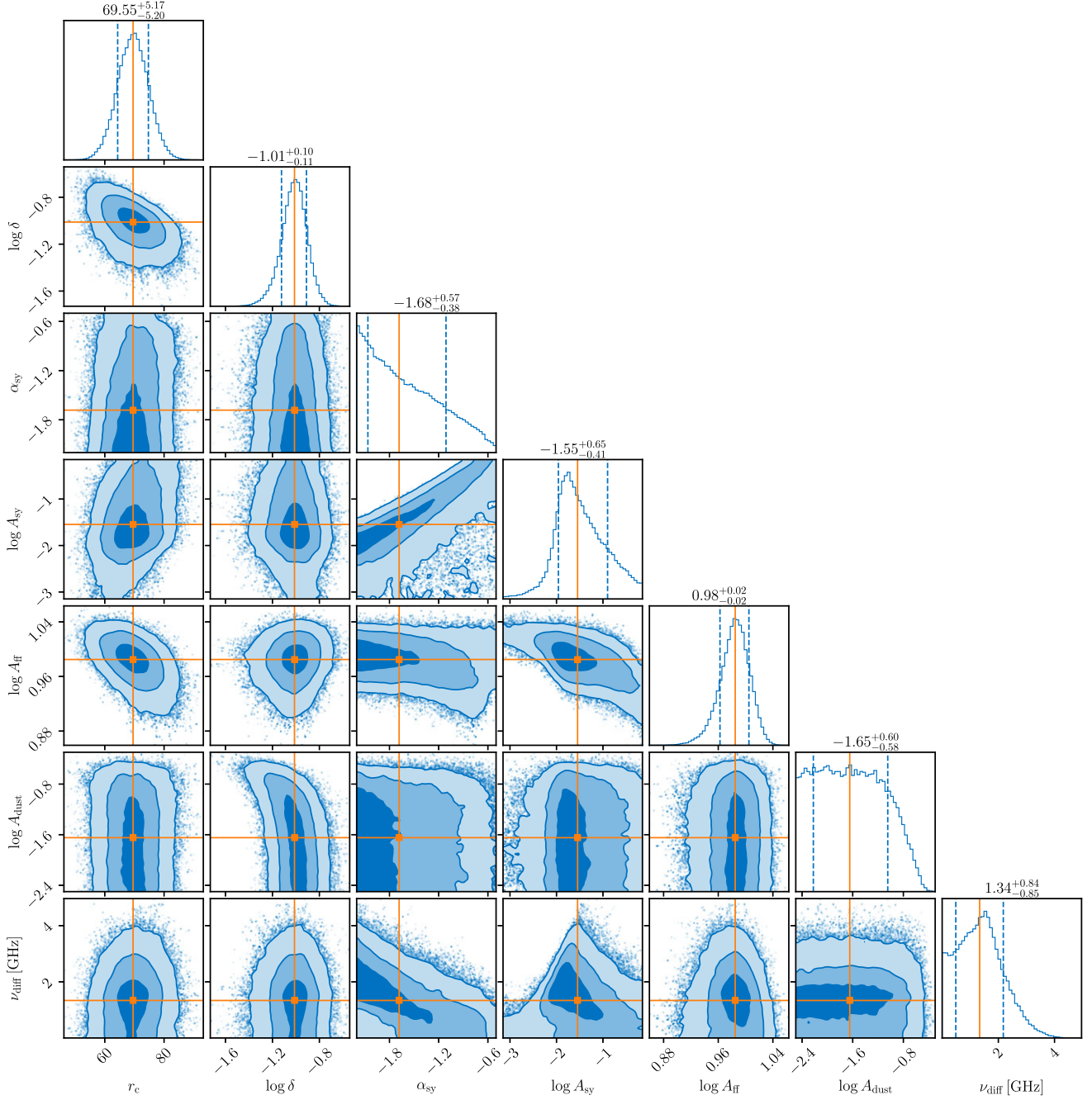
Figure A2. Posteriors of the MCMC fitting in Section 4.1.2 (fit shown in Fig. 2, middle panel). The top panels show the 1D distributions of each parameter, with the orange line marking the position of the median, and the dashed lines the 1σ confidence interval. We note that for α_{sy} and $\log A_{\mathrm{dust}}$ only an upper limit is established.

Figure A3. Posteriors of the MCMC fitting using the clumpy model in Section 4.1.3 (fit shown in Fig. 2, bottom panel). The top panels show the 1D distributions of each parameter, with the orange line marking the position of the median, and the dashed lines the 1σ confidence interval. We note that for $\alpha_{\rm sy}$ and $\log A_{\rm dust}$ only an upper limit is established.

This paper has been typeset from a TEX/LATEX file prepared by the author.